International Forum on Aeroelasticity and Structural Dynamics
IFASD 2017
25-28 June 2017 Como, Italy

CFD-BASED FLUTTER PREDICTION FOR HIGH REYNOLDS NUMBER FLOWS WITH FREE BOUNDARY LAYER TRANSITION

Michael Fehrs[1], **Jens Nitzsche**[1], **Anne Hebler**[1]

[1] DLR - German Aerospace Center
Institute of Aeroelasticity
Bunsenstrae 10, 37073 Göttingen, Germany
Michael.Fehrs@dlr.de

Keywords: boundary layer transition, local correlation-based transition model, airfoil flutter

Abstract: This paper introduces a local, correlation-based transition model used for CFD-based flutter predictions. The presented γ transition model is based on the γ transport equation of the γ-Re_θ transition model. The model is calibrated for external aerodynamic flows in a low turbulence environment and is validated based on experimental data for moderate and high Reynolds numbers found in free flight. A steady 2D validation case, a steady 3D test case for comparison with the e^N method, an unsteady 2D validation test case, and an unsteady 2D test case for comparison with the e^N method are presented. In addition, the effect of a boundary layer transition on the flutter behavior of an airfoil in transonic flow at a free flight Reynolds number is demonstrated.

1 INTRODUCTION

Approximately 55 % of the total drag of a transport aircraft in cruise flight is caused by viscous drag. AIRBUS estimates a potential of a 15 % drag decrease by laminar flow technology and turbulence and separation control [1]. A laminar boundary layer reduces the skin friction drag as the velocity gradient at the wall $du/dy|_w \propto \tau_w$ is lower. In addition, the laminar boundary layer has a lower displacement thickness, which results in a different effective camber of the airfoil or wing (Fig. 1). This change in camber alters the lift and moment of the device (Fig. 2). The increase in lift depends on the extent of laminar flow, which is affected by the airfoil or wing design, the disturbance environment, and the overall flow conditions. A change in the disturbance environment or flight condition can result in a loss of lift as the transition position moves upstream.

In addition to the influence on the aerodynamic forces, the transitional[1] boundary layer flow gives different shock locations and strengths in transonic flow and the separation behavior is changed with the potential of laminar separations. Therefore, transitional flows require aerodynamic and aeroelastic investigations, which include some appropriate transition modeling to capture these effects.

The DLR TAU-Code [2] provides the TAU transition module with an e^N method, based on linear stability theory [3, 4]. The e^N method is widely used for the prediction of Tollmien-Schlichting (TS) and crossflow (CF) transition in flows around transport aircraft configurations. In addition

[1] A boundary layer flow with some relevant extent of laminar flow.

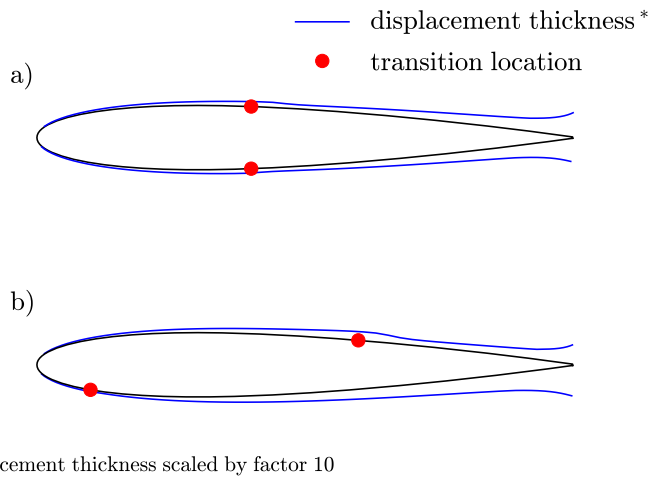

Figure 1: Influence of transition location on the displacement thickness.

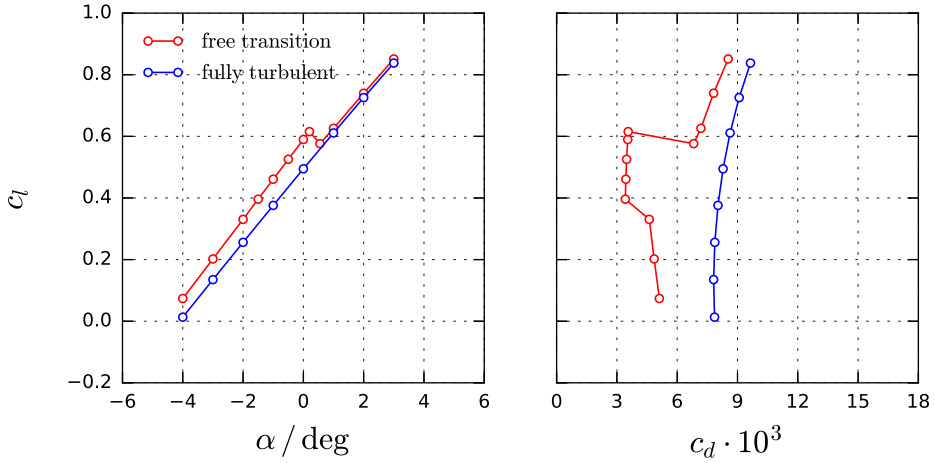

Figure 2: Drag bucket of a laminar airfoil at $Re = 18 \cdot 10^6$.

to the TAU transition module, the γ-Re_θ transition model is available in the TAU code [5]. The γ-Re_θ transition model is a local, correlation-based transition model [6–8]. The transition onset correlation is based on the freestream turbulence level and pressure gradient. Grabe et al. [9] extended the prediction method to crossflow transition in three-dimensional flows.

The γ-Re_θ transition model fails to predict certain external aerodynamic flows: In favorable pressure gradient flows at high Reynolds numbers, the transition onset is predicted too far upstream. The main reason for the wrong prediction is the pressure gradient correlation, which is based on the pressure gradient parameter $\lambda_\theta = (\theta^2/\nu)\cdot(dU/ds)$. Figure 3 depicts the correlation for the transition onset Reynolds number $Re_{\theta t}$ of Langtry & Menter [8] for the γ-Re_θ transition model. The correlation is built to give a similar behavior as proposed by Abu-Ghannam & Shaw [11].

In addition, Fig. 3 depicts the indifference Reynolds number $Re_{\theta,\,ind}$ for incompressible, viscous flow, and spatial disturbance growth [12]. The indifference Reynolds number is the natural stability limit of the laminar boundary layer for Tollmien-Schlichting transition. Any correlation for Tollmien-Schlichting transition has to account for the stability limit as no disturbance growth

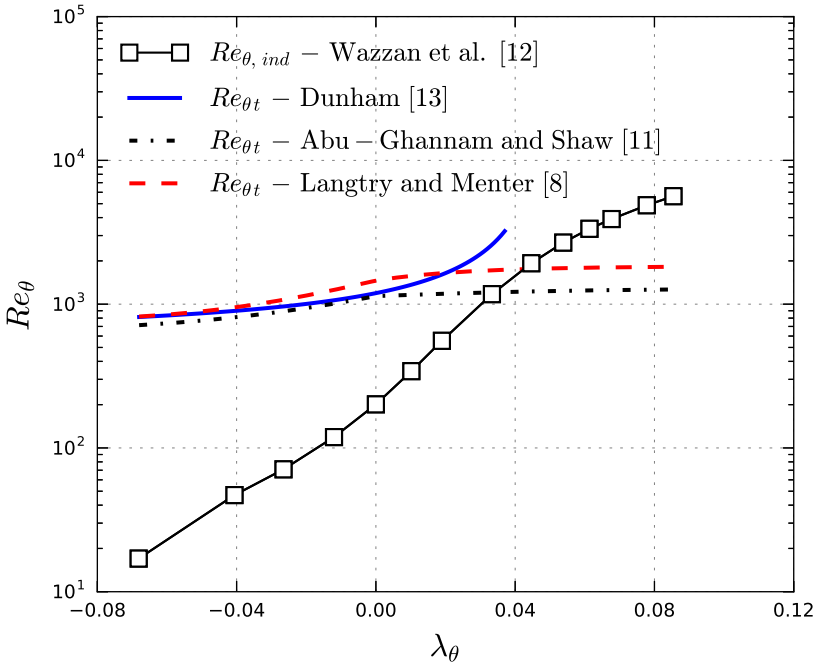

Figure 3: Stability limit and correlations for the influence of pressure gradients on the transition onset.

exists below this Reynolds number (e.g. the correlation by Dunham [13]). The correlation by Abu-Ghannam & Shaw [11] is mainly built for high turbulence flows in turbomachines, for which the main transition mechanism is bypass transition.

The correlations by Langtry & Menter [8] and Abu-Ghannam & Shaw [11] are well suited for these high turbulence flows in turbomachines. However, for flows in a low turbulence environment usually found in free flight with a Tollmien-Schlichting transition mode, a revision of the γ-Re_θ transition model is required. Therefore, a simplified γ transition model with a new onset correlation is presented. The transport equation for the transition onset Reynolds number is dropped to exclude any additional effect given by the $\widetilde{Re}_{\theta t}$ transport. The γ transition model is used to compute the unsteady aerodynamic forces required for flutter prediction in the transonic flight regime.

2 γ TRANSITION MODEL

2.1 Transition Model Description

The γ transition model is built for Tollmien-Schlichting (TS) transition prediction at free flight Reynolds numbers. The γ-Re_θ model is reduced to the γ transport equation to exclude any effect given by the $\widetilde{Re}_{\theta t}$ transport equation. In a next step, the transition onset correlations are revised to account for TS transition at the desired flow conditions. The framework of the γ transport equation of the γ-Re_θ model is kept and all parameters and variables are taken from Langtry & Menter [8] if not stated otherwise.

The transition onset correlation includes the effect of turbulence level and pressure gradients on the transition onset. The freestream turbulence level used in the onset correlation is directly specified by the farfield value, which is in agreement with the choice of a single critical N_{TS} factor. The pressure gradient influence is computed locally inside the boundary layer.

The $\widetilde{Re}_{\theta t}$ transport equation of the γ-Re_θ transition model is replaced by an algebraic equation to compute the momentum loss Reynolds number at transition onset $Re_{\theta t}$. The transport equation for the intermittency variable γ is given by:

$$\frac{\partial \rho \gamma}{\partial t} + \frac{\partial \rho \, u_j \gamma}{\partial x_j} = P_\gamma - E_\gamma + \frac{\partial}{\partial x_j} \left[(\mu + \mu_t) \frac{\partial \gamma}{\partial x_j} \right] \tag{1}$$

The production term P_γ reads:

$$P_\gamma = F_{length} \, \rho \, S \, F_{onset} \, (1 - \gamma) \tag{2}$$
$$\text{with } F_{length} = 14$$

F_{onset} activates the intermittency production once the transition onset Reynolds number $Re_{\theta t}$ is reached:

$$F_{onset} = max \, (F_{onset\,2} - F_{onset\,3}, \, 0) \tag{3}$$

$$F_{onset\,2} = min \, (F_{onset\,1}, \, 2) \tag{4}$$

$$F_{onset\,3} = max \left[1 - \left(\frac{R_T}{2} \right)^3, \, 0 \right] \tag{5}$$

$$F_{onset\,1} = \frac{Re_\nu}{\xi \, Re_{\theta t}} \tag{6}$$

The model is calibrated for a freestream value of $R_T = 1$. The approach by Spalart & Rumsey [14] is used to cancel the turbulence decay in the freestream.

The transition onset Reynolds number $Re_{\theta t}$ is compared to the scaled vorticity Reynolds number Re_ν / ξ [8]. The parameter ξ contains a compressibility correction, based on the compressible, zero-pressure gradient boundary layer equations [15, 16]. The correction is given for the local isentropic Mach number M_e:

$$\xi = a_3 \, M_e^3 + a_2 \, M_e^2 + a_1 \, M_e + a_0 \tag{7}$$
$$\text{with } a_3 = -0.0186, \; a_2 = 0.1569, \; a_1 = 0.0091, \; a_0 = 2.18844$$

The transition onset correlation includes the effect of turbulence level and pressure gradient. The turbulence level τ in % and the acceleration parameter K are used to predict the transition onset Reynolds number $Re_{\theta t}$:

$$Re_{\theta t} = 120 + 380\, k_t\, \tau^{-\frac{2}{5}} \tag{8}$$

The effect of the pressure gradient is given by the factor k_t:

$$k_t = \exp\left\{\left[3.2 - 3.2\, min\left(\sqrt{\tau_\infty},\, 1.0\right)\right] K_t\right\} \tag{9}$$

$$K_t = K \cdot Re \tag{10}$$

$$K = \frac{\nu_e}{U_e^2} \frac{dU_e}{ds} \tag{11}$$

The pressure gradient parameter K is computed based on the isentropic boundary layer edge quantities obtained by the local static pressure. K accounts solely for the local effects of the pressure gradient as no integral boundary layer quantity is included [17]. It is scaled by the Reynolds number as K is inversely proportional to the unit Reynolds number [18]. The factor k_t gives a strong increase of $Re_{\theta t}$ for accelerated flows in a low turbulence environment to agree with the theoretical stability limit for TS transition. For increasing turbulence levels, the effect of the pressure gradient is weaker. The onset correlation is depicted in Fig. 4. In addition, the correlation for the influence of the turbulence level on the transition onset by Mayle [19] is depicted.

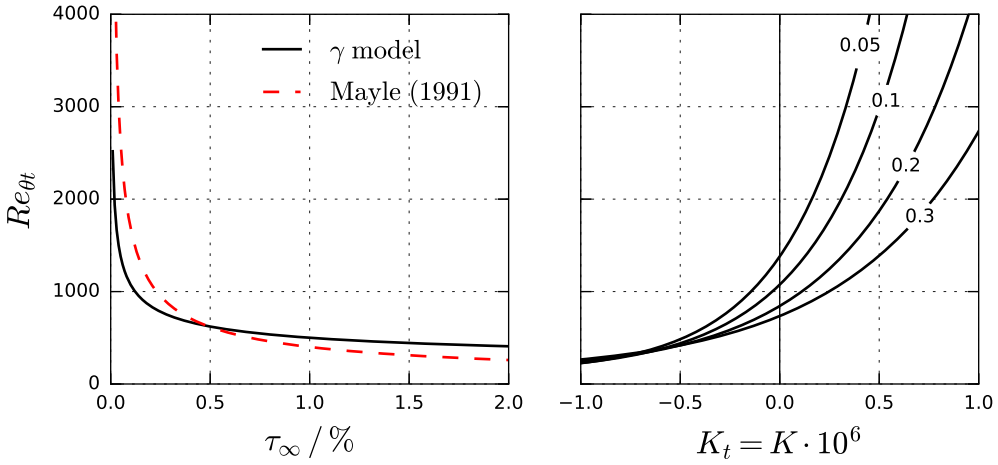

Figure 4: Influence of turbulence level τ and pressure gradient on the transition onset. Line numbers indicate turbulence level.

The destruction term E_γ in equation 1 reads:

$$E_\gamma = c_{a2}\, \rho\, \Omega\, \gamma\, F_{turb}\, \left(c_{e2}\gamma - 1\right) \tag{12}$$

F_{turb} is given by:

$$F_{turb} = F_{turb\,1}\, F_{\theta t} \tag{13}$$

$$F_{turb\,1} = \exp\left[-\left(\frac{R_T}{4}\right)^4\right] \tag{14}$$

The function $F_{\theta t}$ is based on $Re_{\theta t}$ instead of $\widetilde{Re}_{\theta t}$ [20]. The blending based on $F_{\theta t}$ and $F_{turb\,1}$ ensures $F_{turb} = 0$ outside of the boundary layer. The coupling of the transition model to the SST k-ω turbulence model is not changed from [20]. There is no modification to account for laminar separations. The γ transition model can be extended with crossflow correlations described by Grabe et al. [9].

2.2 Calibration and Validation

The calibration of the transition model requires the determination of the transition onset and the scaling of the intermittency production. Both calibration parameters have a high mutual influence as the first intermittency onset and the downstream intermittency production have to result in the right location of the fully turbulent boundary layer. The transition onset is deduced from existing empirical correlations but requires some modification as a certain amount of intermittency is required to change the laminar boundary layer flow. During calibration it is found that a constant F_{length} value is sufficient for most test cases.

To determine the exact onset condition data from Zwaaneveld [21], Braslow & Visconti [22], and McGhee et al. [10] are used. The transition onset correlation is determined for adverse pressure gradient flows at $M = 0.299$, $Re = 1.1 \cdot 10^6$ [21] and favorable pressure gradients at $M = 0.2$, $Re = 30 \cdot 10^6$ [22] for a fixed value of F_{length}. The resulting correlation is tested for two angles of attack from Run 15 [10] to match the flow inside and outside the laminar drag bucket. Once a set of parameters is found, further validation cases are computed.

The first example for a validation case is given in Fig. 5 for the experimental data by McGhee et al. [10]. The drag curves are used for model validation. Table 2.2 depicts the test case data for the experimental runs. Run 15 has to be excluded for validation as two angles of attack are used for the calibration (full red symbol in Fig. 5).

Run	$Re\,/\,10^6$	M	$\alpha_{start}\,/\,\mathrm{deg}$	$\alpha_{end}\,/\,\mathrm{deg}$
3, 4, 6	10	0.12	-3.99	7.16
13	10	0.3	-4.06	8.3
15	9.5	0.4	-3.04	6.26
28	10	0.23	-3.0	6.32

Table 1: Test case data for the NLF(1)-0414F [10].

The NLF(1)-0414F is designed to allow a large extent of laminar flow by accelerating the boundary layer flow on the upper surface up to $x/c \approx 0.7$ in the design range of $c_l = 0.4$ ... 0.45. The leading edge is a compromise between a sharp nose for a wide laminar drag bucket and a blunt nose for improved performance close to $c_{l,\,max}$ [10]. The computations are performed for a turbulence level of $\tau = 0.08$ % based on the information given by McGhee et al. [10]. The experimental data show a laminar drag bucket for all test cases. The γ-Re_θ transition model is

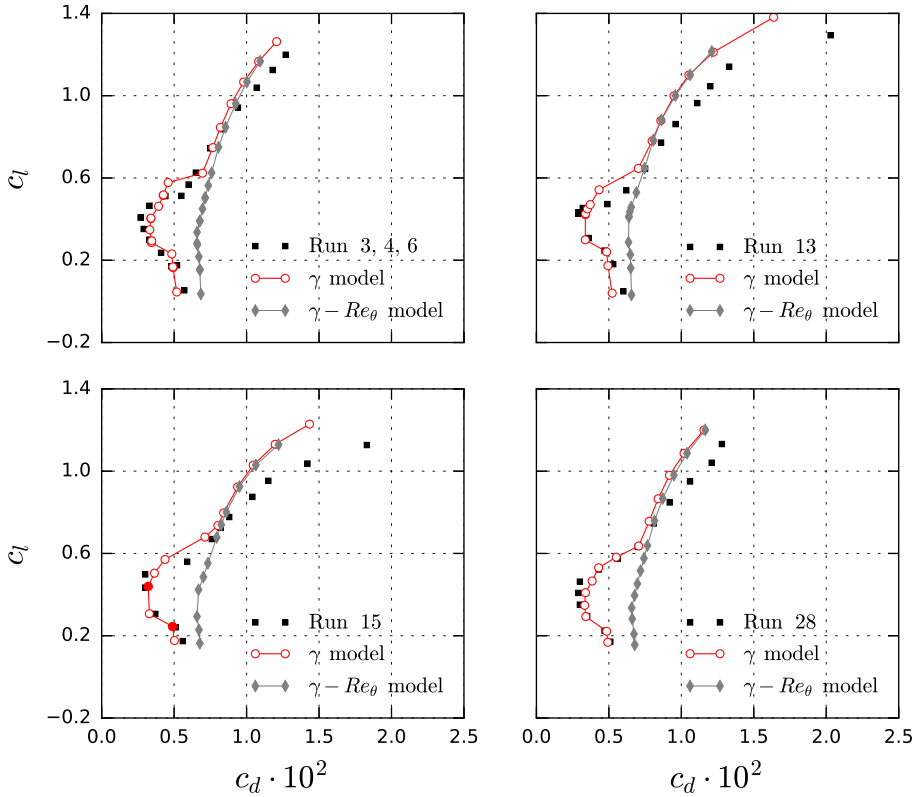

Figure 5: Experimental data by McGhee [10] for the NLF(1)-0414F and transition model predictions

not able to predict the high Reynolds number flows correctly. The γ transition model gives a laminar drag bucket for all test cases. The extent of the drag bucket and the behavior at the drag bucket limit is captured. For high angles of attack, the boundary layer flow shows trailing edge separations in the experiment [10], which are not given by the computational models.

The second test case presented is the forward-swept wing of the ALLEGRA design. The geometry is given by the jig-shape of the ALLEGRA-S FEM model [23]. The natural laminar flow wing has a leading edge sweep angle of $|\Lambda_{LE}| = 17°$. Computations are performed for $Re = 25 \cdot 10^6$, $\alpha = 2°$, and $M = 0.78$ with the γ-Re_θ transition model, the γ transition model, the TAU transition module (e^N method, LILO, SST k-ω model), and the SST k-ω turbulence model. The critical N factors are given by $N_{TS} = 11$ for Tollmien-Schlichting transition and $N_{CF} = 10$ for crossflow transition [24]. For the correlation-based transition model computations, a turbulence level of $\tau = 0.05$ % is used. The critical N_{TS} value and the turbulence level describe a low disturbance environment in free flight.

Figure 6 depicts the skin friction coefficient distribution on the suction side of the ALLEGRA-S wing for the different transition prediction methods. The transition mechanism is Tollmien-Schlichting transition. Therefore, a direct comparison of the different methods is possible. The e^N method and the γ transition model agree well. The γ model gives a more upstream transition onset in the wing inboard region and on the wing tip. The γ-Re_θ transition model is not able to reproduce the transition behavior of the e^N method.

Table 2.2 presents the lift and drag coefficients for the different transition prediction methods and the fully turbulent computation. The drag and lift benefit by a partly laminar flow compared to the fully turbulent solution is clearly given for the e^N method and the γ transition model.

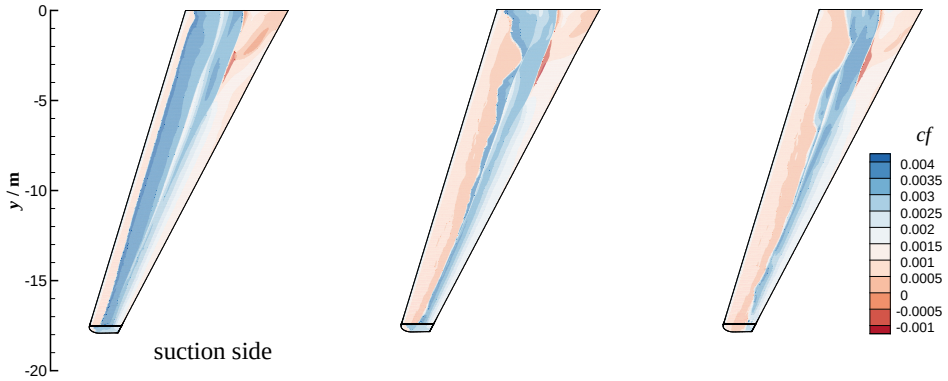

Figure 6: Skin friction coefficient distribution for the suction side of the ALLEGRA-S wing: γ-Re_θ transition model (left), γ transition model (middle) and e^N method (right).

method	C_L	C_D
γ-Re_θ transition model	0.4997	0.01996
γ transition model	0.5458	0.01892
e^N method	0.5514	0.01867
SST k-ω model	0.4887	0.02029

Table 2: Lift and drag coefficients for the ALLEGRA-S wing.

3 RESULTS

3.1 Overview

Boundary layer transition is affected by an unsteady base flow as e.g. the pressure distribution changes or by any unsteadiness in the disturbance environment. Changes in the flow conditions might be periodic or singular events (e.g. gust encounters). Periodic-unsteady transition is of high importance in gas turbines [19], for helicopter rotor blades in forward flight [25], for the design of micro aerial vehicles [26], and for the flutter prediction of airfoils [27, 28].

As Radespiel et al. [26] and Richter et al. [29] point out, there is little published on models for unsteady transition prediction and information on the unsteady transition behavior is often drawn from wind tunnel experiments. One exception is the unsteady e^N method presented by Radespiel et al. [26] and Windte and Radespiel [30]. The difference between a steady and an unsteady transition prediction increases with frequency and large deviations exist for $k = \omega\, c\,/2\,/U_\infty = 1$ for low Reynolds numbers $Re < 10^5$ [30].

As unsteady transition prediction methods are not widely available, most investigations are restricted to steady prediction methods. The γ transition model does not include any explicit assumptions about the unsteady transition process. However, the model is applied to the unsteady base flow and the γ transport equation might provide some intrinsic unsteady behavior. To investigate the model capabilities for unsteady computations, an unsteady validation test case for the supercritical CAST10-2 is presented. In addition, a comparison to the steady e^N method available in TAU is provided. The influence on the flutter behavior is investigated for a 2D test case given by the RAE 2822 at a free flight Reynolds number.

3.2 CAST10-2: Unsteady Validation

3.2.1 CAST10-2: Description

The unsteady transition behavior of the γ transition model is investigated based on experimental data for the CAST10-2. The CAST10-2 is an airfoil designed for a transonic commercial transport aircraft. The section coordinates are documented by Dress et al. [31]. The CAST10-2 has been investigated in the Transonic Wind tunnel Göttingen (DNW-TWG) [27,32]. The DLR project ALLEGRA provides flow measurements at transonic Mach numbers and $Re = 2 \cdot 10^6$. The results for $M = 0.7$, $Re = 2 \cdot 10^6$ are used to validate the unsteady transition behavior at $k = \omega \cdot (c/2)/\, U_\infty = 0.05$. In the computations with the γ transition model, a turbulence level of $\tau = 0.35$ % is used at $M = 0.7$ [33,34].

3.2.2 CAST10-2: Results

Figure 7 depicts the lift and drag coefficients from the ALLEGRA ALF 3 experiment [27] and from the computation with the γ transition model. The experimental lift coefficients are based on the integrated pressure measurements and the drag coefficients are based on wake measurements. The standard deviation of c_l is indicated by the error bars. The small deviation indicates steady flow conditions for all angles of attack investigated in the experiment. The γ transition model predicts the drag bucket correctly.

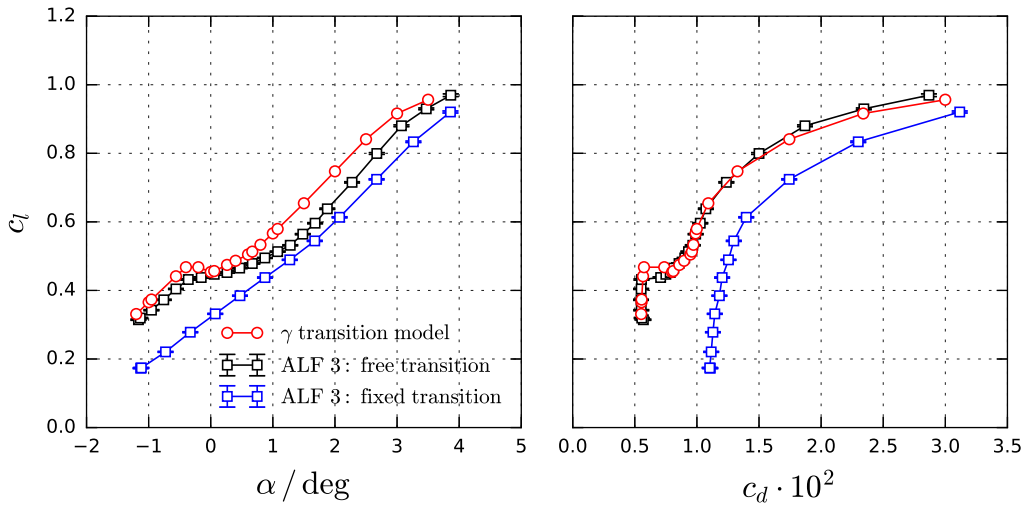

Figure 7: CAST10-2: lift and drag coefficients.

The computational results reproduce the lift curve with a certain offset in angle of attack. No wind tunnel corrections exist for the DNW-TWG, which account for circulation, blockage, or sidewall effects. No model deformation is included in the computation and a farfield condition is used. Hebler et al. [27] use a wind tunnel correction of $\Delta\alpha_{corr} = -0.3°$ and a Mach number correction of $\Delta M_{corr} = -0.01$ to reproduce the steady lift curve at $M = 0.75$ with MSES. A similar angle of attack correction improves the lift curve prediction of the γ transition model further.

Next, the γ transition model is used to compute a harmonic pitch oscillation at $M = 0.7$ for $\overline{\alpha} = 0°$, $\widehat{\alpha} = 0.8°$, and $k = 0.05$. The experimental mean angle of attack is $\overline{\alpha} = 0.034°$. Figure 8 depicts the phase averaged lift coefficients from the ALF 3 experiment (128 data points / period) and for a single pitch period from the γ transition model. The base flow at $\alpha = 0°$ is slightly unsteady in the computation.

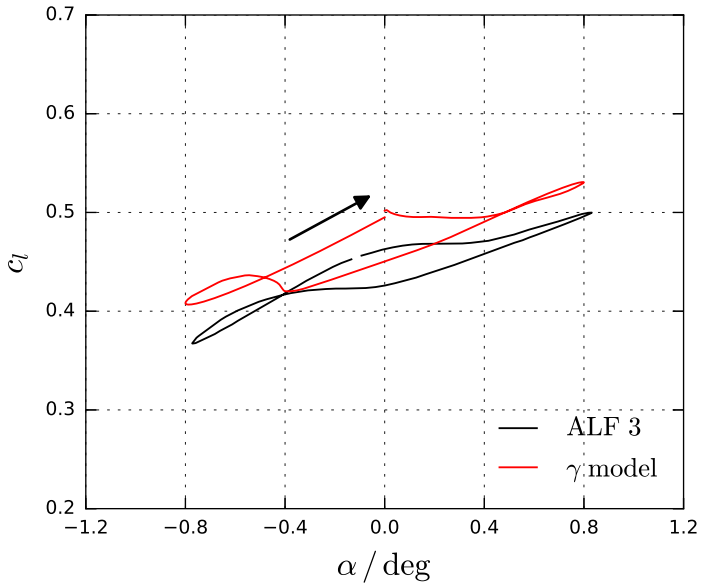

Figure 8: CAST10-2: unsteady lift coefficient for $\overline{\alpha} = 0°$, $\widehat{\alpha} = 0.8°$, and $k = 0.05$.

The experimental and CFD data show an unsteady lift response with nonlinear effects. The experimental data gives a smooth variation of c_l as the transition location changes at the drag bucket limit. The γ transition model gives a more sudden change. The α offset in the steady computation is also present in the unsteady computation.

Figure 9 depicts the transition location over one pitch period from the ALF 3 experiment and the CFD computation. Based on the hot-film sensors along the suction side, laminar, intermittent, and fully turbulent regions are identified. Separated boundary layer flow is read from the pressure sensors. The computational results are evaluated based on the friction coefficient distribution. The peak value of c_f is taken as the location, at which the fully turbulent boundary layer state is reached. This point is referred to as transition location given by the red line in Fig. 9. Any laminar separation is identified by the zero-crossings in the c_f distribution. The separation and reattachment locations are both indicated by circles.

The basic unsteady transition behavior is captured by the γ transition model. Similar to the experimental data, the separation locations do not show a large variation with angle of attack. Separation occurs further downstream in the computation and the size of the separation bubble is smaller. The upstream movement of the transition location is captured. However, the transition locations are not as symmetric for the up- and down-stroke compared to the ALF 3 data. The shock induced separation, which occurs slightly phase-shifted to the maximum deflection of the airfoil in the computation, is not given in the experimental data.

3.2.3 CAST10-2: Summary

The ALF 3 experimental data provide a test case for a high Mach number at a moderate Reynolds number at a low reduced frequency. The computational approach based on farfield conditions results in an offset for the steady test cases. Additional uncertainties in the turbulence level, model deformation, and wind tunnel effects complicate the validation. The lift curve at the drag bucket limit, and to a larger degree the drag coefficients, reproduce the experimental data reasonably well.

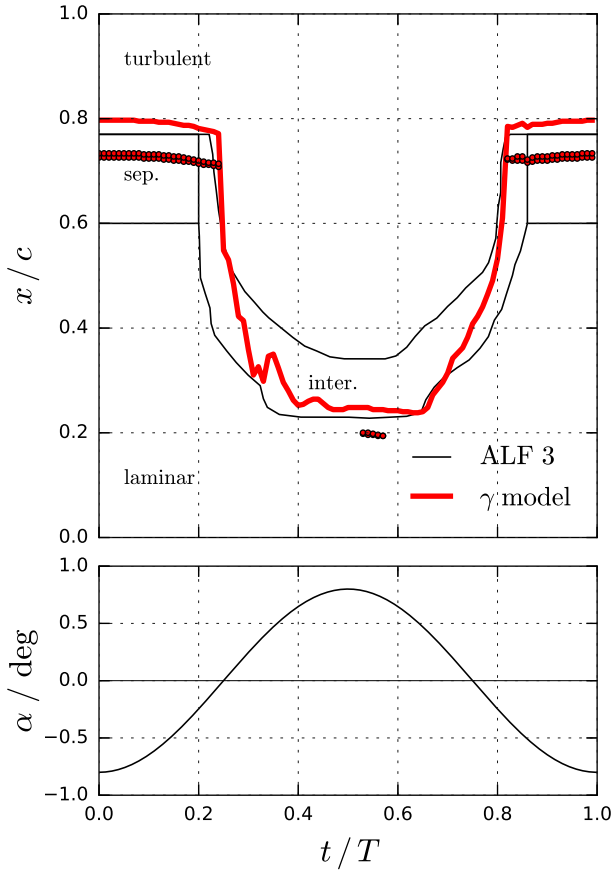

Figure 9: CAST10-2: transition location

The unsteady aerodynamic lift response for a forced pitch motion from the experiment is reproduced by the γ transition model qualitatively. The transition position movement is reproduced by the γ transition model. Some differences exist in the predicted separation behavior. The measurements indicate larger regions of separated flow.

Flutter predictions require the frequency-depending aerodynamics for small excitation amplitudes. A final assessment of the γ transition model based on a single large amplitude test case is not possible. Further computations in the high Mach and Reynolds number range are required, which include frequency and amplitude variations.

3.3 NLF(2)-0415M: γ Model and e^N Method

The γ transition model is applied to the unsteady base flow but does not model any unsteady transition behavior similar to the unsteady method presented by Radespiel et al. [26]. To give some qualitative information on the unsteady behavior, the γ transition model is compared to the steady e^N method of the TAU transition module. For low reduced frequencies, both methods should give similar results for a similar steady state.

A modified NLF(2)-0415 airfoil is considered for this unsteady test case. The rear part of the lower surface is modified to reduce the aerodynamic moment for a wind tunnel test in the DLR ALLEGRA project. The modified model is designated NLF(2)-0415M. The lift curve is computed for a critical N factor $N_{TS} = 12$ and a turbulence level of $\tau = 0.05$ % at $Re = 18 \cdot 10^6$ and $M = 0.38$. The TAU transition module (LILO) and the γ transition model give a stable

transition location inside the laminar drag bucket for $\alpha = -1°$. The pressure and skin friction coefficient distributions for both methods are depicted in Fig. 10. The transition location is further downstream for the e^N method. The difference in the transition location has little effect on the lift coefficient.

Forced pitch motion computations at single frequencies for $k = 0.25$, 0.5, 0.75, and 1 are performed to cover the reduced frequency range for flutter calculations. The amplitude of the sine motion is given by $\widehat{\alpha} = 1° \cdot 10^{-4}$ to obtain a linear lift response. Figure 11 depicts the magnitude and phase of the lift coefficient derivative due to pitch $c_{l\alpha}$ for $\overline{\alpha} = -1°$. In addition, linear system identification results (pulse, Kaiser et al. [35]) are obtained for a maximum amplitude of $\widehat{\alpha} = 1° \cdot 10^{-6}$ for the γ transition model. The single frequency results for both transition prediction methods meet the pulse results.

For both methods, the transition location is very stable on the upper and lower surface. The e^N method gives no variation in the transition location. A refined boundary layer grid can provide a better resolution of any transition location oscillation but gives a strong increase in computational time. In addition to the increase in computational time, a finer grid can result in no stable transition location for the base flow, especially in the case of separation bubbles and shocks. As Krumbein et al. [36] point out, it is not certain for which unsteady flows a steady e^N method is sufficient. A further assessment of the γ transition model requires additional comparisons to the steady and unsteady e^N method.

3.4 RAE 2822: Supercritical Airfoil

3.4.1 RAE 2822: Description

The unsteady test case considered for flutter prediction is the supercritical airfoil RAE 2822 [37] in transonic flow at a free flight Reynolds number. The flow conditions are $\mathit{Re} = 20 \cdot 10^6$, $\mathit{M} = 0.75$ with a turbulence level of $\tau = 0.05$ %. For the unsteady computations, the pulse approach [35] is used for amplitudes of $\widehat{\alpha} = 1° \cdot 10^{-5}$ to 10^{-6} and $\widehat{h} = 10^{-5}$ m to 10^{-6} m. The flutter boundary is obtained by a p-k method [38]. The equation to solve is given by:

$$\frac{U_\infty^2}{b^2}\,[\mathbf{M}]\,p^2 + [\mathbf{K}] - q_\infty\,S\,[\mathbf{A}] = 0 \tag{15}$$

It is assumed, that for harmonic motion in both degrees-of-freedom (pitch and heave), the lift and moment response is linear and harmonic [39]. The eigenvalues p are determined from equation 15, which describe the reduced damping $\delta = \sigma\, b/U_\infty$ and reduced frequency $k = \omega\, b/U_\infty$ based on semi-chord length $b = c/2$:

$$p_1 = \delta_1 + i\,k_1, \qquad p_2 = \delta_2 + i\,k_2 \tag{16}$$

The aerodynamic matrix $[\mathbf{A}]$ depends on the reduced frequency k. The frequency of $[\mathbf{A}(k)]$ has to meet the frequency of the computed eigenvalue p. Therefore, the eigenvalues have to be determined by iteration. Once the matrix $[\mathbf{A}(k)]$ is known for a specific Mach and Reynolds number, the frequency f and reduced damping δ of the aeroelastic system is computed for increasing freestream velocities. The flutter speed is found at zero-damping.

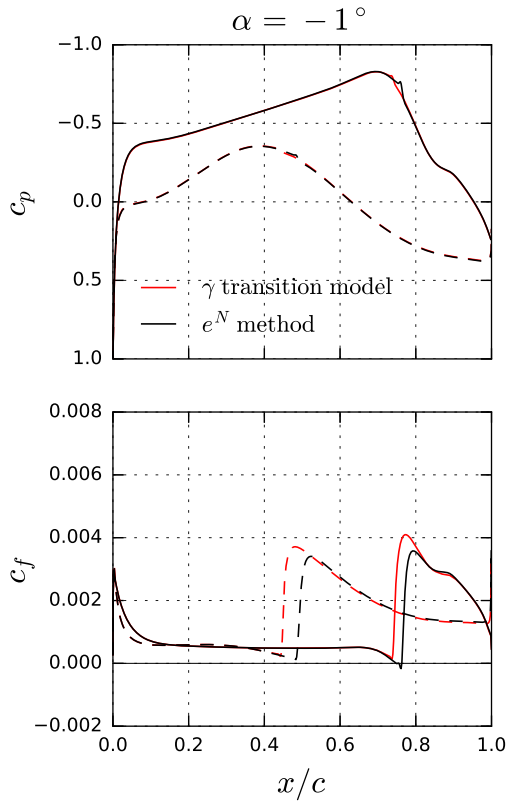

Figure 10: NLF(2)-0415M: Pressure and skin friction coefficient distribution for $\alpha = -1°$.

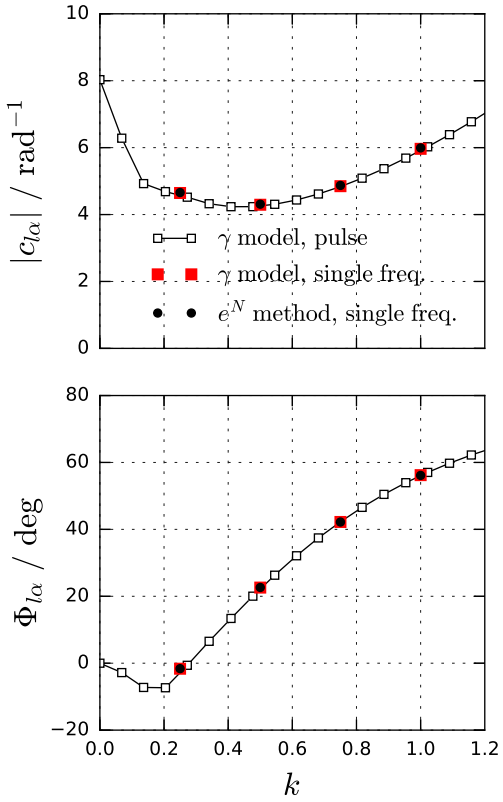

Figure 11: NLF(2)-0415M: Unsteady lift and moment from the γ transition model and e^N method.

The system given by equations 15 is coupled in terms of structural and aerodynamic parameters. Classical bending-torsion flutter requires a mode interaction. The static moment S_α gives a non-diagonal structural matrix $[\mathbf{M}]$. The lift coefficient derivative due to pitch $c_{l\alpha}$ and the moment coefficient derivative due to heave c_{mh} result in a non-diagonal aerodynamic matrix $[\mathbf{A}]$.

3.4.2 RAE 2822: Results

Figure 12 depicts the lift, drag, and quarter-chord moment curve for the transitional and fully turbulent flow computed with the γ transition model. No laminar drag bucket exists as the transition location is far downstream for the whole angle of attack range. For higher angles of attack, the lift stalls and the drag strongly increases as shock-induced separations occur.

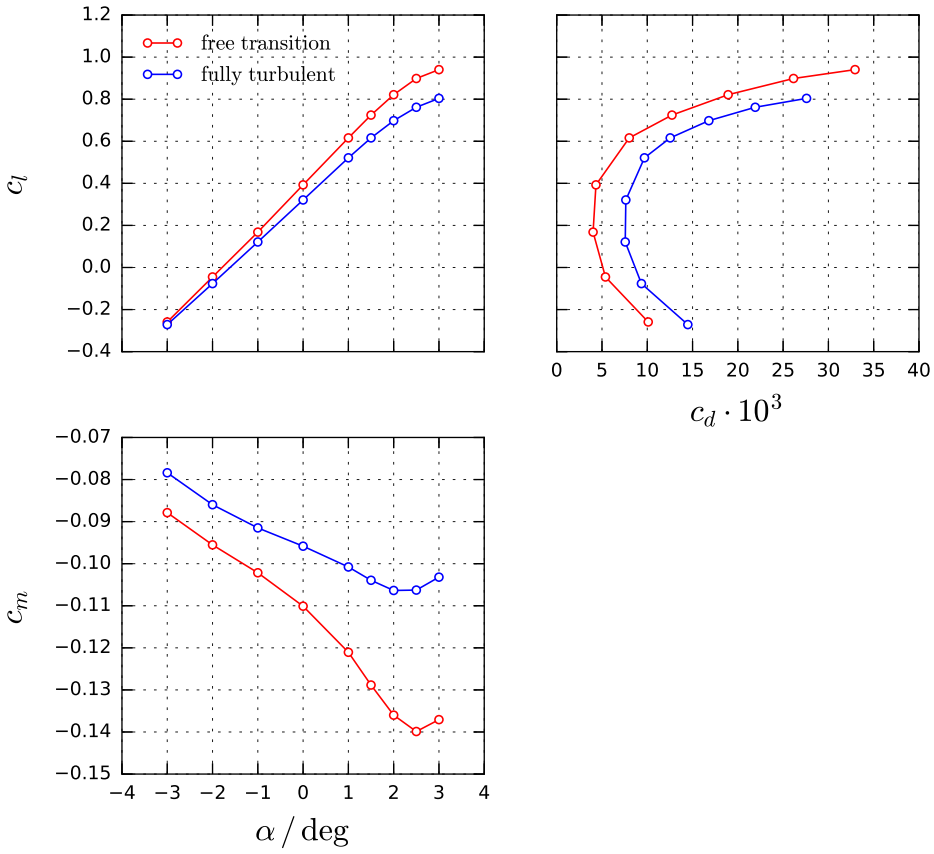

Figure 12: RAE 2822: Lift, drag, and moment curve

For angles of attack $\alpha < 1°$, there is a drag benefit given by the laminar boundary layer flow. For higher angles of attack, the transitional flow encounters stronger shocks with shock-induced laminar separations, which increase the airfoil drag above the fully turbulent drag. The fully turbulent moment coefficient variation is rather linear up to $\alpha = 2°$. The transitional moment coefficient slope $|dc_m/d\alpha|$ increases with angle of attack.

Figure 13 depicts the pressure and skin friction coefficient distribution for $\alpha = 0°$ and $2°$. The critical pressure coefficient is $c_{p,\,crit} = -0.59$. Both flow conditions give a transonic flow on the suction side. The boundary layer is laminar up to the pressure minimum. The downstream adverse pressure gradient causes transition. On a finer gird, the transition zone length increases and there is no c_f increase upstream of the shock. However, the conjunction of the first c_f

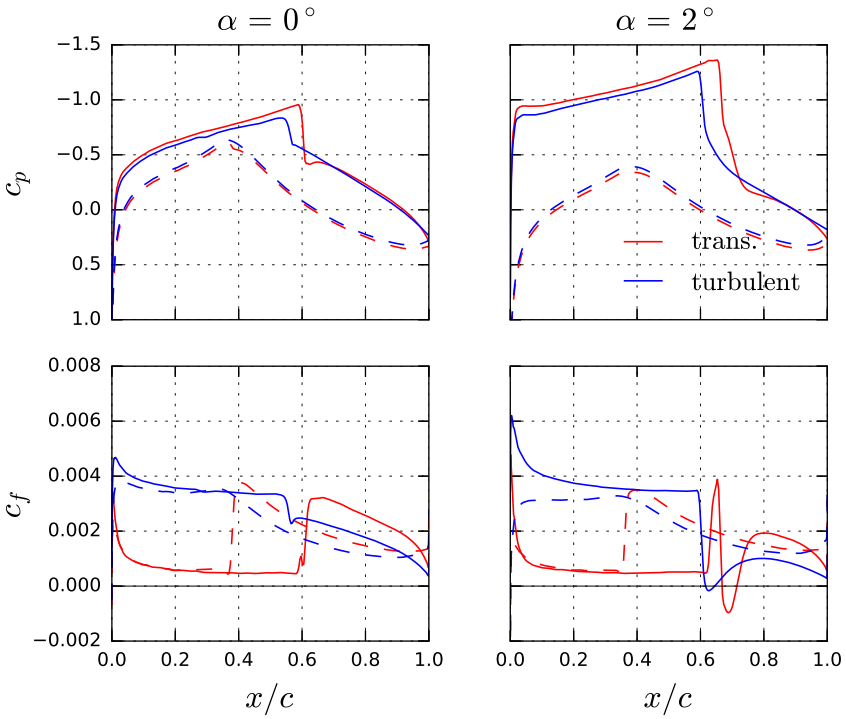

Figure 13: RAE 2822: Pressure and skin friction distribution for $\alpha = 0°$ and $2°$.

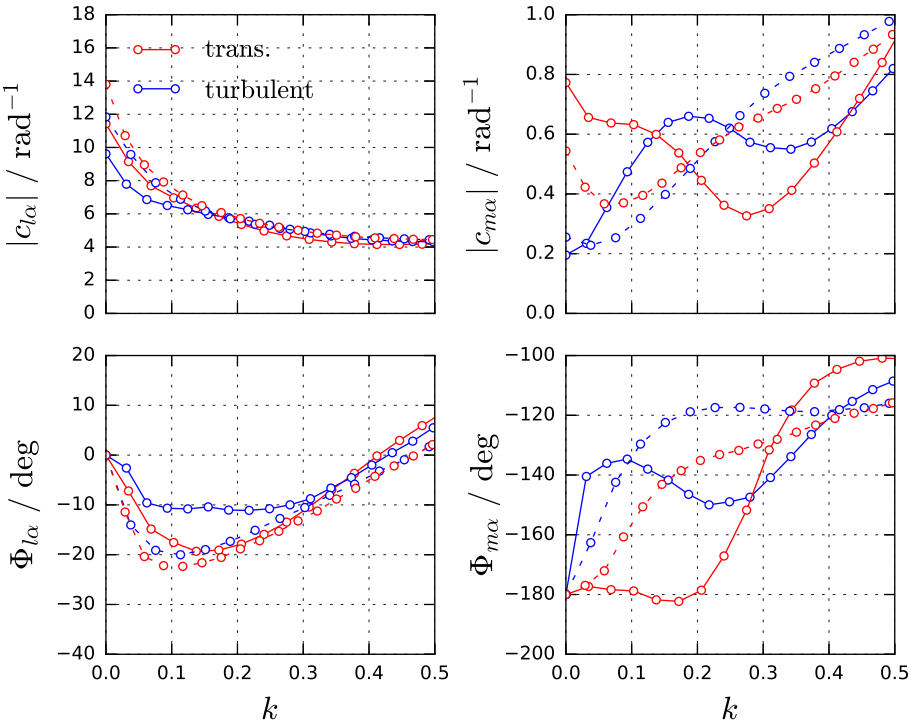

Figure 14: RAE 2822: Unsteady lift and moment for $\overline{\alpha} = 0°$ (dashed) $\overline{\alpha} = 2°$ (full) due to pitch.

increase and the shock location does not alter the unsteady results for the given flow conditions.

Figure 14 depicts the unsteady pitch results for the mean angles of attack $\overline{\alpha} = 0°$ and $2°$ for a fully turbulent and a transitional flow. There is a pronounced difference in magnitude and phase for the unsteady aerodynamic moment between both angles of attack and the fully turbulent and transitional flow condition. The transitional flow at $2°$ gives a phase lead of the aerodynamic moment with $\Phi_{m\alpha} < -180°$, which enables a 1-dof flutter of the pitch mode. A similar phase lead is shown for the supercritical CAST10-2 airfoil in a wind tunnel experiment with free transition by Hebler et al. [27] and numerically by Fehrs et al. [28].

The unsteady aerodynamic data for pitch ($\partial c_l/\partial\alpha$, $\partial c_m/\partial\alpha$) and heave ($\partial c_l/\partial h$, $\partial c_m/\partial h$) is used to build the aerodynamic matrix $[\mathbf{A}] = f(M, Re, k)$ for a flutter calculation. An arbitrary structural model is chosen to move the reduced frequency at flutter below $k = 0.3$ to demonstrate the effect of the changed unsteady aerodynamics in this frequency range. The structural parameters are given in Tab. 3.4.2. There is no structural damping included in the model.

$x_\alpha = S_\alpha/(mc)$	$r_\alpha = \sqrt{I_\alpha/(m\,c^2)}$	ω_α/ω_h	f_h / Hz	m / kg	c / m
0.03	0.2	0.7	15	50	1

Table 3: Structural parameters for flutter investigation.

	transitional			fully turbulent		
$\overline{\alpha}$ / deg	mode	U_{fl} / (m/s)	k_{fl}	mode	U_{fl} / (m/s)	k_{fl}
0	1	189.7	0.265	1	179.8	0.278
2	1	313.7	0.169	1	230.2	0.226

Table 4: RAE 2822: Flutter results.

The flutter speed and reduced frequency at flutter is given in Tab. 3.4.2. Figure 15 depicts the frequency and damping for the given structural model. The first heave-dominated mode gets unstable in all cases. In the case of $\overline{\alpha} = 0$, the fully turbulent flow and the transitional flow show a similar flutter behavior. As the angle of attack is increased, the flutter speed of the transitional flow increases strongly. The frequencies of both modes converge but the interaction stabilizes the system compared to the fully turbulent flow.

3.4.3 RAE 2822: Summary

A transonic, free-flight Reynolds number test case is presented for the RAE 2822. The transitional flow has a pronounced effect on the shock position, the shock strength, and the separation behavior. The lift curve for both types of flow is linear up to the drag divergence given by shock induced separations. Only minor differences exist in the unsteady lift in magnitude and phase. At the same time, the unsteady aerodynamic moment of the transitional flow differs strongly from the turbulent state. The phase lead of the moment coefficient due to pitch enables a 1-dof flutter. For the 2-dof system, the flutter behavior changes strongly for the flow with free boundary layer transition. As an arbitrary structural model is used, the results can not be generalized. However, the investigation stresses the importance of the effect of free transition as the unsteady aerodynamics are strongly altered by the laminar flow region.

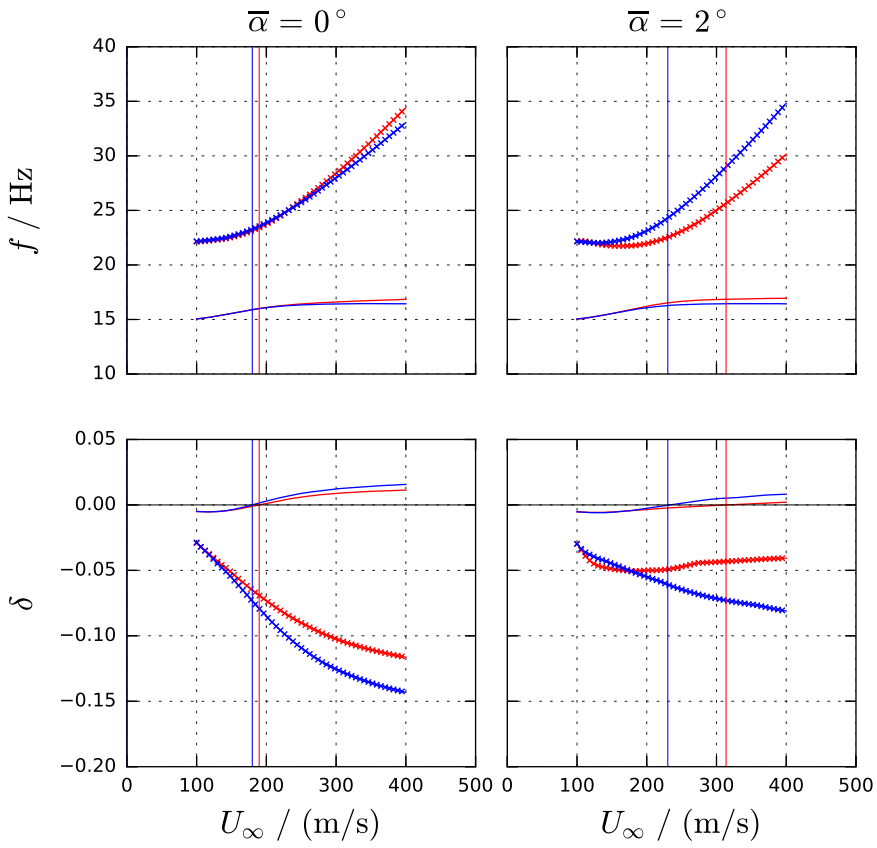

Figure 15: RAE 2822: frequency and damping at $\overline{\alpha} = 0°$ and $\overline{\alpha} = 2°$.

4 CONCLUSION

This paper introduces a local, correlation-based transition model used for CFD-based flutter predictions. The presented γ transition model is based on the γ transport equation of the γ-Re_θ transition model. The model is calibrated for external aerodynamic flows in a low turbulence environment and is validated based on experimental data for moderate and high Reynolds numbers found in free flight. The γ-Re_θ transition model fails for favorable pressure gradient flows in a low disturbance environment as the transition onset correlation violates the theoretical stability boundary.

A steady 2D validation test case for the NLF(1)-0414F is presented, for which the drag bucket is predicted reasonably well with the γ transition model. In addition, a steady 3D test case for comparison with the e^N method is presented. The γ transition model is able to reproduce the Tollmien-Schlichting transition predicted by the e^N method. For flutter calculations, the unsteady transition behavior has to be captured. In a first validation step, the experimental data for the CAST10-2 airfoil at a moderate Reynolds number is used. The γ transition model is able to determine the transition location variation with angle of attack. Second, a comparison to the e^N method is used to investigate the transition prediction capabilities at higher reduced frequencies demonstrating a similar unsteady behavior as the steady e^N method.

A transonic flutter test case at a free flight Reynolds number is used to demonstrate the effect of boundary layer transition on the flutter stability. Transition changes the shock position, strength, and the separation behavior at the shock, which can result in a very different flutter speed as it is shown for the given test case. Once airfoils and wings with large laminar flow regions are

considered, valid and robust transition models are required. The γ transition model is well suited for aeroelastic, CFD-based investigations. However, further unsteady validation test cases are required for a final assessment of the model.

Acknowledgments: This work is funded by DLR programmatic research in the DLR project *VicToria*.

5 REFERENCES

[1] Schrauf, G., Gölling, B., Wood, N. (2006). KATnet – Key Aerodynamic Technologies for Aircraft Performance Improvement. *5th Community Aeronautical Days*, Wien.

[2] Schwamborn, D., Gerhold, T., Heinrich, R. (2006). The DLR TAU-code: Recent Applications in Research and Industry. In: *Proc. European Conference on Computational Fluid Dynamics ECCOMAS*, Egmond aan Zee.

[3] Krumbein, A., Krimmelbein, N., Schrauf, G. (2009). Automatic Transition Prediction in Hybrid Flow Solver, Part 1: Methodology and Sensitivities. *Journal of Aircraft*, 46(4), 1176–1190.

[4] Krumbein, A., Krimmelbein, N., Schrauf, G. (2009). Automatic Transition Prediction in Hybrid Flow Solver, Part 2: Practical Application. *Journal of Aircraft*, 46(4), 1191–1199.

[5] Seyfert, C., Krumbein, A. (2010). Evaluation of a Correlation-Based Transition Model and Comparison with the e^N Method. *40th Fluid Dynamics Conference*, AIAA, Chicago.

[6] Menter, F. R., Langtry, R. B., Likki, S. R., Suzen, Y. B., Huang, P. G., Völker, S. (2006). A Correlation-Based Transition Model Using Local Variables – Part I: Model Formulation. *Journal of Turbomachinery*, 128(3), 413–422.

[7] Langtry, R. B., Menter, F. R., Likki, S. R., Suzen, Y. B., Huang, P. G., Völker, S. (2006). A Correlation-Based Transition Model Using Local Variables – Part II: Test Cases and Industrial Applications. *Journal of Turbomachinery*, 128(3), 423–434.

[8] Langtry, R. B. and Menter, F. R. (2009). Correlation-Based Transition Modeling for Unstructured Parallelized Computational Fluid Dynamics Codes. *AIAA Journal*, 47(12), 2894–2906.

[9] Grabe, C., Nie, S., Krumbein, A. (2016). Transition Transport Modeling for the Prediction of Crossflow Transition. *34th AIAA Applied Aerodynamics Conference*, AIAA, Washington D.C..

[10] McGhee, R. J., Vikne, J. K., Pfenninger, W., Beasley, W. D. (1984). Experimental Results for a Flapped Natural-Laminar-Flow Airfoil with High Lift/Drag Ratio. Tech. Rep. TM-85788, NASA.

[11] Abu-Ghannam, B. J., Shaw, R. (1980). Natural Transition of Boundary Layers - The Effects of Turbulence, Pressure Gradients, and Flow History. *Journal of Mechanical Engineering Science*, 22(5), 213–228.

[12] Wazzan, A. R., Okamura, T. T., A. M. O. Smith, A. M. O. (1968). Spatial and Temporal Stability Charts for the Falkner-Skan Boundary-Layer Profiles. Tech. Rep. DAC-67086, McDonnell Douglas Astronautics Co..

[13] Dunham, J. (1972). Predictions of Boundary Layer Transition on Turbomachinery Blades. In: *Boundary Layer Effects in Turbomachines*, AGARD-AG-164, AGARD, 57–71.

[14] Spalart, P. R., Rumsey, C. L. (2007). Effective Inflow Conditions for Turbulence Models in Aerodynamic Calculations. *AIAA Journal*, 45(10), 2544–2553.

[15] Criminale, W. O., Jackson, T. L., Joslin, R. D. (2003). *Theory and Computation in Hydrodynamic Stability*. 1st ed., Cambridge: Cambridge University Press.

[16] Mack, L. M. (1965). Computation of the Stability of the Laminar Compressible Boundary Layer. In: *Methods in Computational Physics Vol. 4* Academic Press, 247–299.

[17] Mislevy, S. P., Wang, T. (1995). The Effects of Adverse Pressure Gradients on Momentum and Thermal Structures in Transitional Boundary Layers: Part 1 - Mean Quantities. In: *ASME 1995 International Gas Turbine and Aeroengine Congress and Exposition*, ASME.

[18] Schreiber, H. A., Steinert, W., Küsters, B. (2002). Effects of Reynolds Number and Free-Stream Turbulence on Boundary Layer Transition in a Compressor Cascade. *Journal of Turbomachinery*, 124(1).

[19] Mayle, R. E. (1991). The Role of Laminar-Turbulent Transition in Gas Turbine Engines. *Journal of Turbomachinery*, 103, 509–537.

[20] Langtry, R. B. (2006). A Correlation-Based Transition Model Using Local Variables for Unstructured Parallelized CFD Codes. Ph.D. Dissertation, University Stuttgart, Stuttgart.

[21] Zwaaneveld, J. (1979). NLR 7301 Airfoil. *Experimental Data Base for Computer Program Assessment*, AGARD-AR-138, AGARD.

[22] Braslow, A. L., Visconti, F. (1948). Investigation of Boundary-Layer Reynolds Number for Transition on an NACA $65_{(215)} - 114$ Airfoil in the Langley Two-Dimensional Low-Turbulence Pressure Tunnel. Tech. Rep. TN-1704, NACA.

[23] Klimmek, T. (2014). ALLEGRA Meilensteinbericht M 3.3.1 – Definition von Simulationsszenarien für die Böenanalyse der ALLEGRA Konfiguration. Tech. Rep. IB 232-2014 J 08, DLR.

[24] Seitz, A., Kruse, M., Wunderlich, T., Bold, J., Heinrich, L. (2011). The DLR Project LamAiR: Design of a NLF Forward Swept Wing for Short and Medium Range Transport Application. In: *29th AIAA Applied Aerodynamics Conference*, AIAA.

[25] Leishman, J. G. (2000). *Principles of Helicopter Aerodynamics*. 1st ed., Cambridge: Cambridge University Press.

[26] Radespiel, R., Windte, J., Scholz, U. (2007). Numerical and Experimental Flow Analysis of Moving Airfoils with laminar Separation Bubbles. *AIAA Journal*, 45(6), 1346–1356.

[27] Hebler, A., Schojda, L., Mai, H. (2013). Experimental Investigation of the Aeroelastic Behavior of a Laminar Airfoil in Transonic Flow. In: *Proc. IFASD 2013*, IFASD, Bristol.

[28] Fehrs, M., van Rooij, A. C. L. M., Nitzsche, J. (2015). Influence of Boundary Layer Transition on the Flutter Behavior of a Supercritical Airfoil. *CEAS Aeronautical Journal*, 6(2), 291–303.

[29] Richter, K., Koch, S., Gardner, A. D., Mai, H., Klein, A., Rohardt, C. H. (2014). Experimental Investigation of Unsteady Transition on a Pitching Rotor Blade Airfoil. *Journal of the American Helicopter Society*, 59(012001), 1–12.

[30] Windte, J., Radespiel, R. (2008). Propulsive Efficiency of a Moving Airfoil at Transitional Low Reynolds Numbers. *AIAA Journal*, 46(9), 2165–2177.

[31] Dress, D. A., Johnson, J. B., McGuire, P. D., Stanewsky, E., Ray, E. J. (1983). High Reynolds Number Tests of the CAST 10-2/DOA 2 Airfoil in the Langley 0.3-Meter Transonic Cryogenic Tunnel - Phase I. Tech. Rep. TM-84620, NASA.

[32] Mai, H., Hebler, A. (2011). Aeroelasticity of a Laminar Wing. In: *Proc. IFASD 2011*, IFASD, Paris.

[33] Fehrs, M. (2015). Erweiterte Auswertung des Turbulenzgrads aus der TWG-Messkampagne 2011. Internal Presentation. DLR, Institute of Aeroelasticity.

[34] Meyer, R., Sebastian Hakansson, S., Liesner, K. (2012). Turbulenzgradmessungen im DNW-TWG 2011. Tech. Rep. DLR-IB-92517-12/B4, DLR.

[35] Kaiser, C., Thormann, R., Dimitrov, D., J. Nitzsche, J. (2015). Time-Linearized Analysis of Motion-Induced and Gust-Induced Airloads with the DLR TAU Code. In: *Deutscher Luft- und Raumfahrtkongress 2015*, DGLR, Rostock.

[36] Krumbein, A., Krimmelbein, N., Seyfert, C. (2011). Automatic Transition Prediction in Unsteady Airfoil Flows Using an Unstructured CFD Code. In: *29th AIAA Applied Aerodynamics Conference*, AIAA, Honolulu.

[37] Cook, P. H., McDonald, M. A., Firmin, M. C. P. (1979). Aerofoil RAE 2822 - Pressure Distributions, and Boundary Layer and Wake Measurements. In: *Experimental Data Base for Computer Program Assessment*, AGARD-AR-138, AGARD.

[38] Hassig, H. J. (1971). An Approximate True Damping Solution of the Flutter Equation by Determinant Iteration. *Journal of Aircraft*, 8(11), 885–889.

[39] Försching, H., Tichy, L. (2014). Grundlagen der Aeroelastik. In: *Handbuch der Luftfahrzeugtechnik*, München: Hanser Verlag.

COPYRIGHT STATEMENT

The authors confirm that they, and/or their company or organization, hold copyright on all of the original material included in this paper. The authors also confirm that they have obtained permission, from the copyright holder of any third party material included in this paper, to publish it as part of their paper. The authors confirm that they give permission, or have obtained permission from the copyright holder of this paper, for the publication and distribution of this paper as part of the IFASD-2017 proceedings or as individual off-prints from the proceedings.